



Corrosion Performance of Sn-Doped AlCrFeNiMn High-Entropy Alloy Synthesized via Arc-Melting Technique

Praise Mpofu¹ · Nicholas Malatji¹ · Mxolisi B. Shongwe¹ · Lehlogonolo R. Kanyane¹

Received: 17 August 2023 / Revised: 13 September 2023 / Accepted: 18 September 2023 / Published online: 26 October 2023
© The Author(s) 2023

Abstract

Failure of materials such as steels during engineering applications can result in economic harm; hence, developing new corrosion-resistant materials is critical. In this work, high-grade powders of Al, Cr, Fe, Mn, and Ni were used to synthesize an equimolar AlCrFeNiMn high-entropy alloy (HEA) for potential chemical industry application. The cast alloy's properties were further altered by the addition of 1at%, 3at%, and 5at% tin (Sn) as alloying additives. To assess the impact of Sn on the alloy's resistance to corrosion, potentiodynamic polarization tests were conducted in various acidic and basic environments. Several surface inspection techniques, including scanning electron microscopy (SEM), optical microscopy (OPM), X-ray diffractometry (XRD), and energy-dispersive X-ray spectroscopy (EDS), were employed to examine the morphological changes and elemental composition of the alloy after it was subjected to corrosive conditions. The nano-indentation machine was used to analyze the materials' nanohardness. TGA analysis was also performed to determine how Sn additions affected the AlCrFeNiMn HEA's thermal stability. In 0.5 M HCl solution, the Sn-doped alloys demonstrated good corrosion resistance. Their exposure to 0.5 mol/L H₂SO₄ solution, on the other hand, found to be deleterious to their electrochemical stability. The weight loss of 5 at% Sn-doped samples in 0.5 M H₂SO₄ solution was found to be substantially reduced. The mass of all the samples stayed constant in 3.5 wt% NaOH solution.

Keywords High-entropy alloys · Microstructure · Nano-indentation and corrosion

1 Introduction

Corrosion is a significant issue in several industries, including the automotive, energy, aerospace, and marine sectors [1, 2]. It could lead to material degradation, structural collapse, as well as monetary losses. As a result, new materials with improved corrosion resistance are always needed. The class of metallic materials known as HEAs was first identified in 2004 by Yeh, Lin [3], and his research group at National Tsing Hua University in Taiwan. The peculiar composition of high-entropy alloys, which usually consists of a number of elements with atomic percentages that are about equal or close to equal, makes them stand out from other materials. HEAs are generally made to deviate from traditional alloy

design methods, which focus on one or a few key constituents [2].

A novel concept in the creation of alloys with five or more principal components and each element blended in an equimolar ratio or near to one is the concept of HEAs [4]. FeCrMnNiCo and AlCoCrFeMnNi are two examples [5]. Instead of forming complex phases or intermetallic compounds, HEAs frequently consist of a single-solid solution, which distinguishes them from typical alloys. Strong-mixing entropies and sluggish diffusion, which further lessen the material's brittleness, are mostly to blame for this [2, 6].

HEAs are desirable for a variety of applications in the aerospace, energy, automotive, biomedical, and electronic sectors thanks to their distinctive features. The design and optimization of HEAs are a difficult undertaking since the characteristics of HEAs can vary significantly depending on their precise composition, microstructure, and processing circumstances [7]. Because of its superior oxidation resistance, high thermal stability, and exceptional mechanical properties including thermal fatigue and high-temperature strength, HEAs are successfully employed in

✉ Praise Mpofu
mpofupraise9@gmail.com

¹ Department of Chemical, Metallurgical and Materials Engineering, Tshwane University of Technology, P.M.B. X680, Pretoria, South Africa

high-temperature applications [2, 5]. Their exceptional qualities and reasonable pricing have affected the applications of everything from large, well-known structures, bridges, buildings, and automobiles to small, sophisticated kitchen appliances, everyday cooking utensils, and medical devices [8].

There are several methods of synthesizing high-entropy alloys (HEAs), including powder metallurgy, laser cladding, electrodeposition, arc melting, and mechanical alloying [9]. Each of these methods has its advantages and disadvantages, and the choice of method depends on the specific requirements of the application and the properties of the desired alloy [10]. Currently, casting and arc melting are used to create the alloys in the majority of papers on HEAs. According to Li et.al.[11], HEAs costs might be greater than most ordinary alloys because the elements being added to the alloys are very expensive, for example, W, Nb, Cr, Ti, Co, V, and Ni and their diameters are limited; therefore, research on high-performance HEA films and coatings on inexpensive metal substrates has also interested many researchers [11]. Varalakshmi et.al, [12] used mechanical alloying to synthesize the AlFeTiCrZnCu. They found out that the HEAs created by mechanical alloying had good compositional uniformity and crystallite sizes of around 10 nm. In comparison to HEAs created by casting, those created by mechanical alloying and consolidation have larger pore densities [13]. According to the investigation done by Ye et.al,[14], conventional techniques and laser cladding both produce Al_x-FeCoNiCuCr alloys with the same phase composition.

Yin et al. [15] explain that HEAs have better resistance to corrosion than many types of commonly used stainless steel because their crystal structures tend to be simpler. For instance, in 1 mol/L NaCl and 0.5 mol/L H₂SO₄ solutions, the high-entropy alloy Cu_{0.5}NiAlCoCrFeSi demonstrated better resistance to corrosion compared to stainless steel [15]. Chen et.al, [16] studied high-entropy alloys' electrochemical characteristics and microstructure are comparing to those of type 304 stainless steel. The authors discovered that HEA exhibited the least corrosion resistance when the concentration of chlorine was 0.5 M. According to the cyclic polarization conducted tests, the absence of hysteresis proved that high-entropy alloys just like steel, are not vulnerable to corrosion when using 1 M H₂SO₄ without chloride ions [16].

The ability of the material to be resistant to corrosion is often changed through elemental alloying. By altering the elemental segregation and phase structure, affecting the quality of the passive film and affecting the kinetics of dissolution, alloying with different elements can have an impact on how the materials resist corrosion [17]. Shi et.al [17] investigated the effects of alloying, together with Cu, Mo, and Al addition on the HEAs corrosion behavior in sulfuric acid. The pitting potential was found to be less likely in

the absence of Cl than in the solution containing chloride. According to the investigations done by Shi et.al. [18], it was found out that there was an increase in corrosion-current density (*I*_{corr}) and a decrease in corrosion potential (*E*_{corr}) as the Al quantity was increased, with increasing Al, indicating the diminished resistance to general corrosion in the solution. Polat et.al [19] explained that low levels of Sn segregation combine with a dense, uniform oxide film that has a good shielding effect to increase the alloy's corrosion resistance. Further enhancing the alloy's corrosion resistance is the formation of a thick SnO₂ oxide film within the corrosion product film on its surface [20].

Among other HEAs, the AlCrFeNiMn alloy has showed excellent physical and mechanical properties, making it a desirable candidate for a number of applications [21]. The discovery and advancement of AlCrFeNiMn HEA, as well as other high-entropy alloys, have opened up new possibilities for material design and engineering [21, 22]. Scientists are actively working to improve the composition, microstructure, and processing of high-entropy alloys to enhance their properties and explore new applications in structural materials, aerospace, energy, and other fields [23].

Sn is commonly added to AlCrFeNiMn HEA in order to enhance certain properties or modify the alloy for a specific use [24]. Testing the AlCrFeNiMn alloy's corrosion resistance in various corrosive environments, particularly in basic and acidic conditions, is important to establish whether it is acceptable for usage in practical applications. The study's findings may improve understanding of how AlCrFeNiMn HEA could react to corrosion when Sn is added. In sectors where exposure to basic and acidic environments is widespread, the knowledge gathered from this study can direct the development of materials that are more resistant to corrosion and assist in the design of more durable components.

2 Experimental

Al, Cr, Fe, Mn, and Ni high-grade powders were employed to make an equimolar AlCrFeNiMn HEA. A tube mixer was used to ensure homogeneity of the material. The material was further compressed using a tablet press and then arc melted in a furnace. Argon gas with high purity was utilized to make the furnace environment more inert, and the Cu crucibles were rotated to ensure chemical homogeneity. As-cast ingots of 20 mm in diameter and 10 mm in height were divided into sections. The characteristics of the cast alloy were further modified by adding 1 at%, 3 at%, and 5 at% Sn as alloying additives. The microstructural evolution and phase composition of the cast and modified HEA were studied using an energy-dispersive spectrometer (EDS) equipped scanning

electron microscope (SEM), X-ray diffraction (XRD), and optical microscopy (OPM). The nanohardness of the samples was assessed using the STEP 4 platform TTX-NHT3 Nano-indenter from the Surface Engineering Research Laboratory, which employs a micro-compression technique to investigate the mechanical characteristics of the different phases in the material. The samples' corrosion behavior was examined using potentiodynamic polarization in five different mediums including 0.5 M of HCl, 0.5 M H₂SO₄, 3.5 wt% NaCl, 0.5 M NaOH, and 0.5 M Na₂SO₄. The weight loss was also run for five weeks in various solution media. Prior to being weighed, the metal samples underwent preparatory grinding and polishing before being immersed in test solutions of NaCl, H₂SO₄, and NaOH. Every seven days, the samples were removed from the test solutions, cleaned, and weighed. Statistical modeling was done on the weight loss results.

3 Results and Discussion

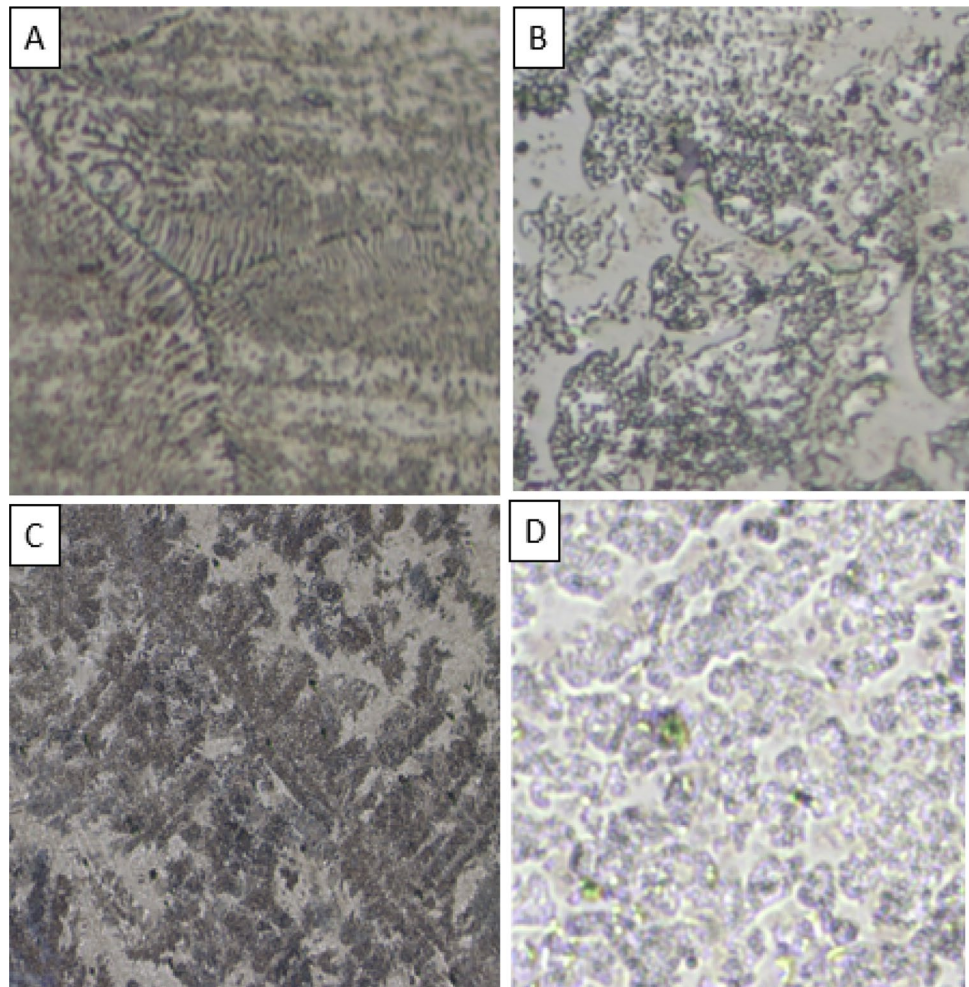
3.1 Phase Formation and Microstructural Evolution

3.1.1 OPM Analysis Results

The optical micrographs of the Sn-doped AlCrFeNiMn HEAs with different percentages of Sn are shown in Fig. 1. The control shows the optical micrograph of the pure AlCrFeNiMn HEA with dendrite structures. It was observed that the addition of 1 at% Sn promoted microstructure refinement of the grains. This may be because tin atoms have the potential to serve as grain refiners, facilitating the development of fine grains in the alloy [25].

When solidifying and cooling processes take place, tin may produce fine intermetallic precipitates that serve as heterogeneous nucleation sites for grain formation. These tiny precipitates have the ability to efficiently pin the borders of the grains, preventing grain development and producing a fine microstructure [26].

Fig. 1 The optical micrographs of control AlCrFeNiMn HEA and Sn-modified samples AlCrFeNiMn HEA with different Sn percentages: **A** control **B** 1 at% Sn, **C** 3 at% Sn, and **D** 5 at% Sn



The grain growth increased with the addition of 3 at% Sn. Slower cooling rates may be to blame for this. Tin can potentially modify the alloy's microstructure and precipitation behavior, which could result in a different behavior [27]. It is likely that the nature or shape of the precipitates created at this greater tin concentration differs from those at 1 at% tin. The grain boundaries may not be sufficiently pinned by these new precipitations, enabling the grains to move and consolidate and leading to an increase in grain expansion thus reducing the hardness of the alloy sample [28].

Grain refining was seen at 5 at% tin. This may be due to the occurrence of a distinct set of precipitates or modifications in the precipitation behavior, which would result in grain refinement. Greater hardness and strength may result from the refined grain structure, since smaller grains improve the efficiency of solid solution strengthening and impede dislocation movement [29, 30]. The particular precipitates that occur at this level of tin concentration may also have a strengthening impact on the alloy, adding to its enhanced hardness [29].

3.1.2 SEM/EDS Evolution

SEM micrographs of AlCrFeMnNi HEA with different Sn percentages are shown in Fig. 2. Three separate phases, shown as white, gray, and black dots on the micrograph, can be seen in the microstructure of the 1 at% Sn sample. Gray spots predominate in the microstructure, and bigger asymmetrical gray particles surround extremely small asymmetrical gray particles, suggesting that these phases make up a greater volume proportion of the alloy's composition.

Figure 3 shows the EDS Micrographs of the AlCrFeMnNi HEA with different tin. According to EDS, Ni-Mn-Sn is abundant in the white phase. These phases are known for their great thermal stability and may tolerate high temperatures without experiencing substantial change in structure [28, 30]. In situations where the material is subjected to high temperatures, this feature is essential. These phases also possess magnetic characteristics [31]. Fe-Cr-Mn is abundant in the phase of gray big particles. Fe-Cr-Mn-rich phases have remarkable corrosion resistance, particularly in hostile conditions like acids and solutions containing chlorides [32]. Chromium and manganese increase the material's capacity to create a shielding oxide layer, which prevents corrosion. They are appropriate for use in chemical processing, oil and gas production, and marine settings because of this feature [33]. The gray tiny particles are a phase rich in Ni-Fe-Cr. These phases are known to have remarkable resistance to corrosion [34]. The combination of chromium and nickel and chromium provides a protective oxide layer which inhibits corrosion in high-temperature, acids and alkaline environments. These characteristics make them appropriate for

use in the petrochemical, marine, and chemical processing industries [35].

As the percentage of Sn increases to 3 at%, three distinct phases are also observed. However, it was demonstrated that the white phase was growing in size and enclosing the gray phase. Several black dots were seen scattered around the microstructure. The white phase is a Ni-Mn-Sn-rich phase. These phases are known for their great thermal stability and may tolerate high temperatures without experiencing substantial change in structure [32, 36]. In situations where the material is subjected to high temperatures, this feature is essential. These phases also possess magnetic characteristics [37].

The gray phase is a Ni-Mn-Al-rich phase. The black spot is an Al-Mn-Ni-rich phase. Al-Mn-Ni phase is known for having a generally low density due to the presence of aluminum a lightweight metal [38]. This quality qualifies them for uses in the automotive, transportation, and aerospace sectors, where weight reduction is sought. These phases are also known to show strong corrosion resistance, especially in some conditions like saltwater and industrial atmospheres [39]. This qualifies them for uses such as naval structures, chemical processes, and outdoor buildings where corrosion resistance is crucial [40].

At 5 at% Sn, three distinct phases were also observed. Only a few black spots, with a larger volume of the white phase, are circling around the gray phase. There is almost a uniform distribution of the gray and white phases throughout the microstructure. The white phase contains the Sn-Ni-Mn-rich phase. The gray phase is a Cr-Ni-Mn-rich phase. This phase may display a combination of ductility and high strength [41]. When nickel and manganese are present, they can aid in strengthening processes, giving rise to materials with better mechanical qualities. They are, therefore, excellent for structural applications where it is necessary for both strength and toughness [42].

3.1.3 XRD Results

Figure 4 shows the XRD patterns of different AlCrFeMnNi HEA samples, control, 1 at% Sn, 3 at% Sn, and 5 at% Sn. The XRD shows that the control AlCrFeMnNi HEA sample consists of combination of BCC FCC, and intermetallic phases. 1 at% Sn sample consists of only BCC phases. 3 at% Sn consists of only BCC phases. This may be because tin tends to promote the formation of BCC (body-centered cubic) or HCP (hexagonal close-packed) structure [43]. BCC has excellent flexibility and great strength. However, despite having a single high strength or toughness single FCC or BCC phase, they are constrained by their incompatibility.

High strength and hardness are balanced by multiphase HEAs, which also have further application possibilities [44]. 5 at% Sn consists of a combination of intermetallic,

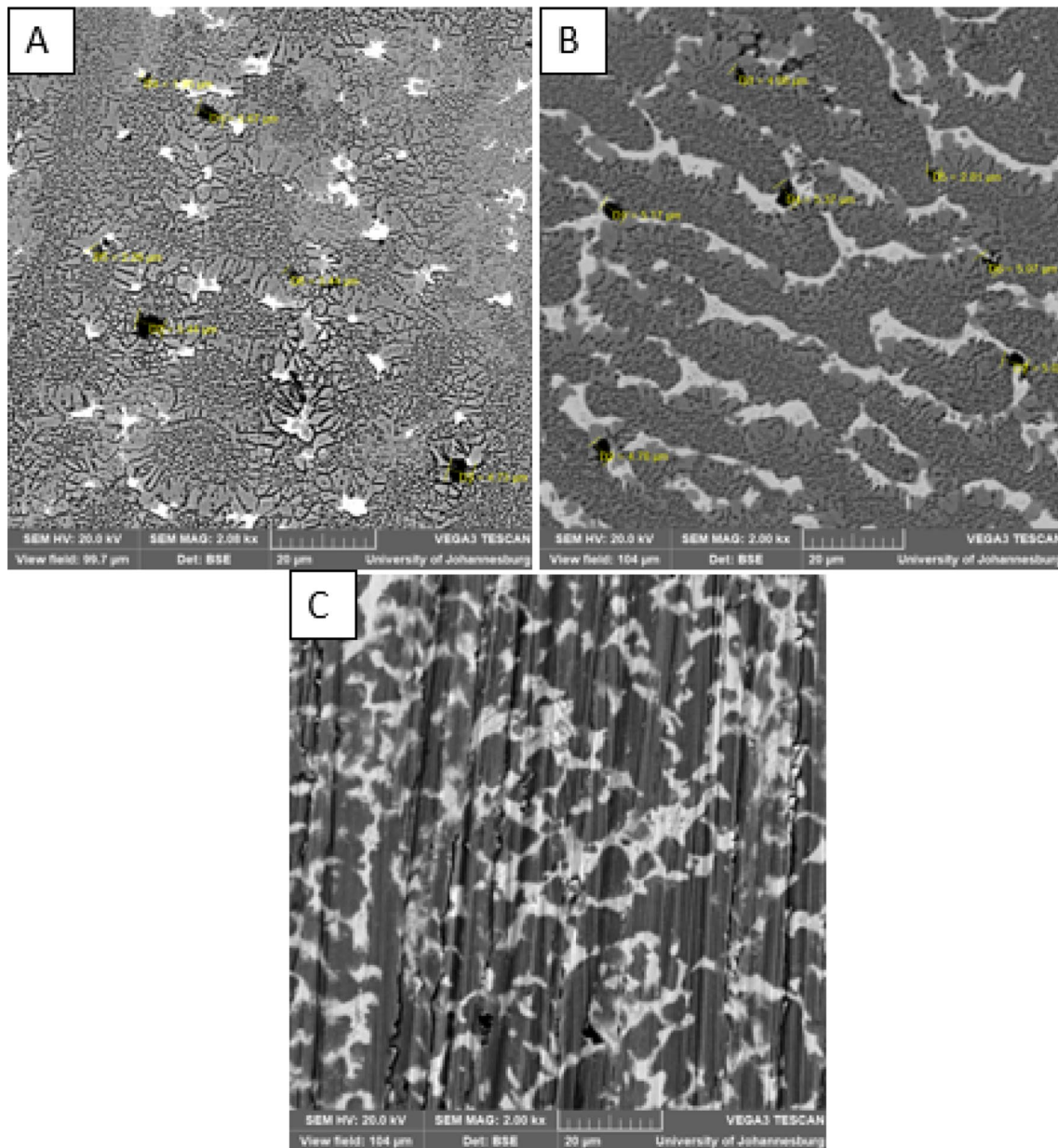


Fig. 2 SEM micrographs of AlCrFeMnNi HEA with different Sn percentages: **A** 1 at% Sn, **B** 3 at% Sn and **C** 5 at% Sn

FCC, and BCC phases. The BCC phase's presence can aid in the FCC phase's stabilization at high temperatures, enhancing the material's high-temperature strength and creep resistance. The presence of tin atoms can boost the alloying elements' interactions, resulting in a strengthening effect [36]. It was observed that with an increase in Sn percentage, the intermetallic (AlSn) and FCC phases are formed confirming the research of [31, 36, 45].

3.1.4 Nano-indentation Results

The addition of 1 at% Sn causes the displacement value to shift to the positive while the elastic modulus value changes further to the negative, as can be seen from the plot of load–displacement curves of specimens in Fig. 5. The displacement value and lowest elastic modulus are more strongly shifted in the positive direction by 5 at% Sn

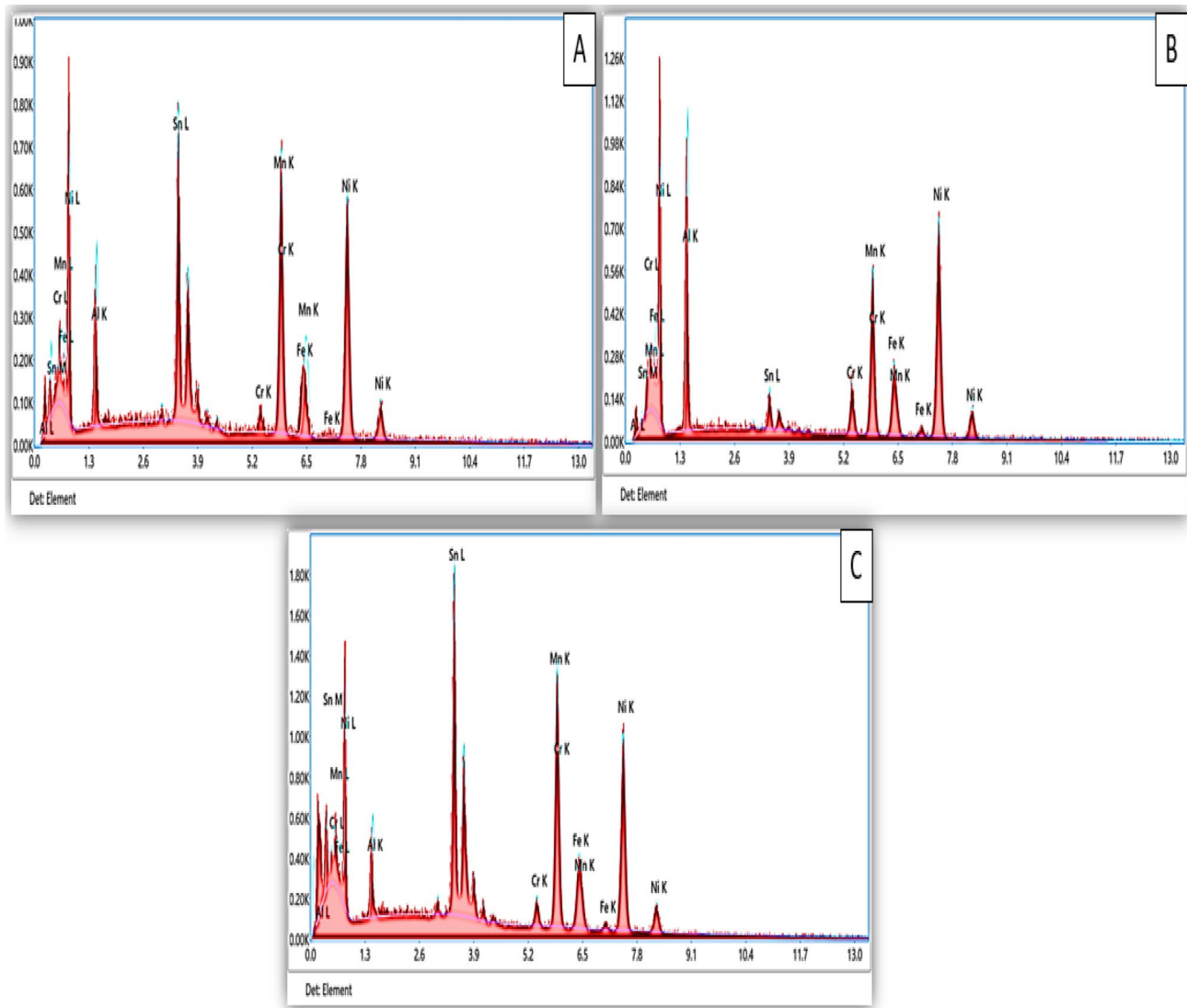


Fig. 3 EDS micrographs of the AlCrFeMnNi HEA with different Sn percentages: **A** 1 at% Sn, **B** 3 at% Sn, and **C** 5 at% Sn

addition. Table 1 shows the hardness, elastic modulus, and displacement data from nano-indentation.

The 5 at% Sn sample had the lowest displacement value of 1668.98 nm, indicating that it has the strongest strength and restricts the passage of indenter forces through the alloy sample [30, 46]. The displacement is negatively shifted by 3 at% Sn, which also has the largest displacement (1668.98 nm) and lowest elastic modulus (159.14 GPa). This demonstrates that there is a decrease in strength, while the elasticity also decreases, permitting the movement dislocations under indentation stresses [30].

Figure 6 shows the plot of penetration depth against time for AlCrFeNiMn HEA and the modified alloy samples with 1 at% Sn, 3 at% Sn, and 5 at% Sn. The penetration depth of 5 at% Sn alloy was observed to be lower as compared to 1 at% and 3 at% Sn-modified AlCrFeNiMn HEA. This may

be due to the fact that a higher solid solution tin content of 5 at% can increase solid solution strengthening, resulting in increased hardness and decreased nano-indentation test penetration depth [30]. This is also made feasible by the fact that the 5 at% tin alloy has a more refined microstructure than the 1 at% and 3 at% tin alloys, which results in increased hardness and a reduced nano-indentation test penetration depth [46].

4 Electrochemical Behavior

4.1 H₂SO₄ Solution

Figure 7 depicts the cathodic and anodic polarization curves of HEAs with 1 at% Sn, 3 at% Sn, and 5 at% Sn additions in

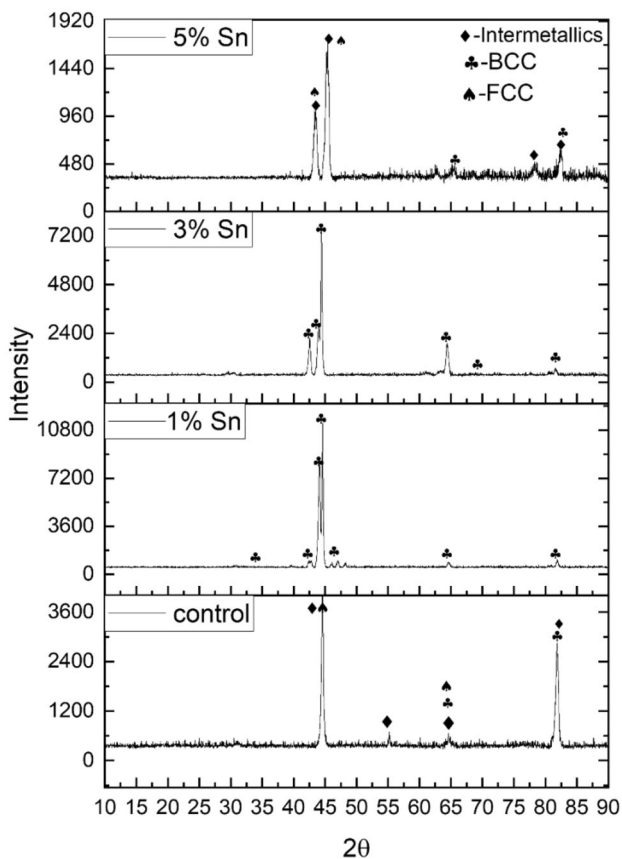


Fig. 4 XRD results for AlCrFeMnNi HEA with different Sn percentages

Table 1 Summarized nano-indentation data for control HEA and Sn-containing samples

Sample	Hardness (Hv)	Elastic modulus (GPa)	Displacement (nm)
Control	728.5	171.57	1647.82
1 at% Sn	623.38	127.64	1817.15
3 at% Sn	541.36	144.9	1881.47
5 at% Sn	722.35	159.14	1668.98

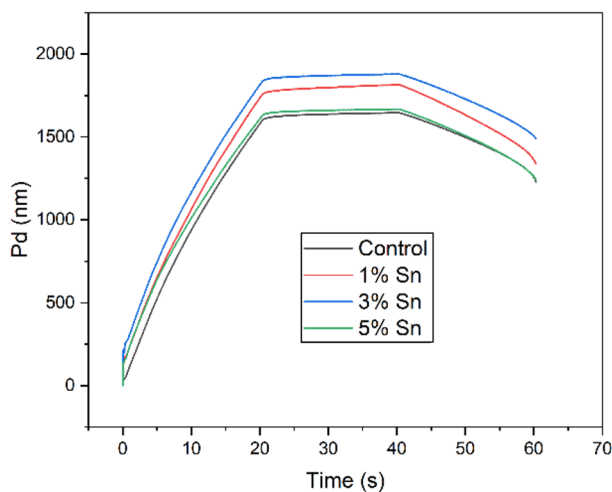


Fig. 6 Penetration depth as a function of time for Sn-modified HEAs

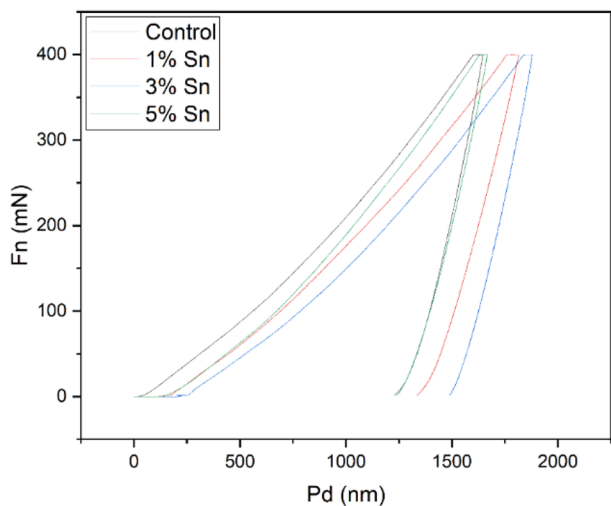


Fig. 5 The plot of load–displacement curves of the control HEA against Sn additions

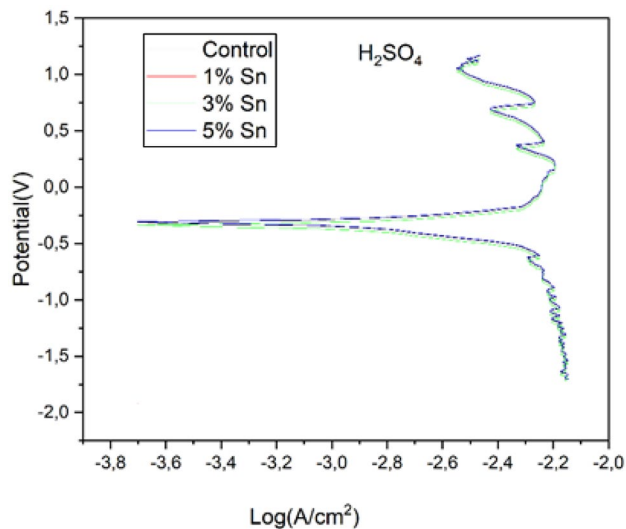


Fig. 7 Potentiodynamic polarization curves of AlCrFeMnNi control HEA and HEAs with 1 at% Sn, 3 at% Sn, and 5 at% Sn additions in 0.5 M H₂SO₄ solution at room temperature

contrast to the control HEA. The Tafel experimental data, performed in 0.5 M H₂SO₄ solution for all four samples, are shown in Table 2. The polarization resistance (R_p)

Table 2 Electrochemical properties of HEAs with 1 at% Sn, 3 at% Sn, and 5 at% Sn additions in comparison with the control HEA when polarized in 0.5 mol/L H₂SO₄ solution at room temperature

	E _{corr} (V)	i _{corr} (A/cm ²) × 10 ⁻⁵	Corrosion rate (mm/year)	Polarization resistance (Ω)
Control	-0.31663	695.18	0.178	3491.5
1 at% Sn	-0.37327	14.899	0.07313	5709.83
3 at% Sn	-0.33983	10.351	0.03028	6912.74
5 at% Sn	-0.32746	0.67014	0.01787	8041.6

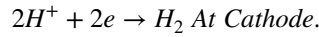
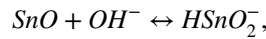
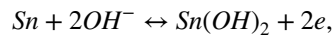
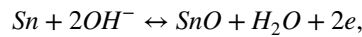
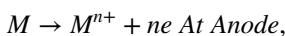
was calculated using Tafel slopes (b_c and b_a) and current densities while the corrosion rate (C_R) was determined for samples using corrosion-current density values, equivalent weight, and density (e and ρ), as shown in equations below [47–49];

$$R_p = \frac{b_c \times b_a}{2.303 \times i_{corr} (b_a + b_c)},$$

$$C_R = 0.13 \times i_{corr} \left(\frac{e}{\rho} \right).$$

With the addition of 1 at% Sn, the potential shifted negatively than that of the control HEA. However, there was a more negative shift in the current density, showing a rise in the alloy surface's resistance to current flow and, consequently, a rise in corrosion resistance. When Sn content increases, the potential switches to the positive, as evidenced by a decrease in HEA corrosion rate. Alloy samples doped with 1 at% and 3 at% Sn had lower corrosion rate compared to the control HEA.

However, 5 at% Sn additive alloy had a much lower corrosion rate than all of the other alloys, hence, higher resistance to corrosion. This is shown by both higher E_{corr} (-0.32746 V) and smaller i_{corr} (6.7014E-06 A/cm²), which indicates that it may have better corrosion resistance compared to the ones with 3 at% Sn and 1 at% Sn and also in comparison with the control HEA. All this is demonstrated by its smaller value of corrosion rate of 0.01787 mm/year. The control HEA had a high corrosion rate value of 0.178 mm/year which was shown to decrease in other alloys with the addition of Sn. The reason for this is Sn causing HEA samples to develop stable passive layers that resist contact with H⁺ ions, making them substantially more corrosion resistant. Cr and Mn elements present increase the material's capacity to create a shielding oxide layer, which prevents corrosion [33].



4.1.1 HCl Solution

Comparing the electrochemical behavior of HEA samples with different Sn additions, Fig. 8 shows the cathodic and anodic polarization curves. The Tafel and cyclic polarization data are shown in Table 3.

With a rise in the value of Sn, there was a positive shift in the potential value and a negative shift in the current density value, signifying a decrease in the rate of corrosion. The sample with 5 at% Sn additions had both higher E_{corr}

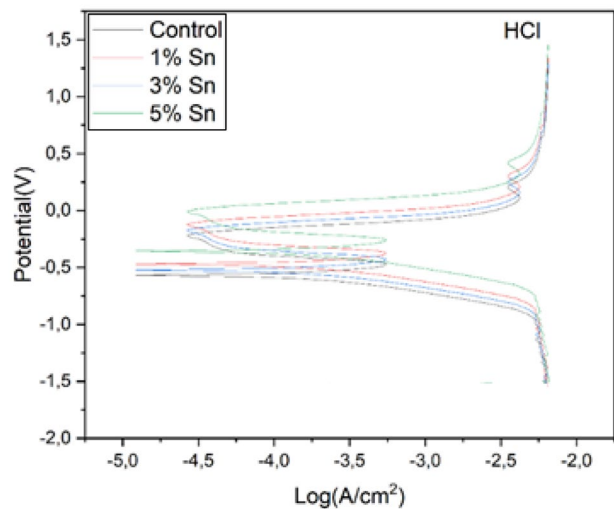


Fig. 8 Potentiodynamic polarization Curves of AlCrFeMnNi Control HEA and HEAs with 1 at% Sn, 3 at% Sn, and 5 at% Sn additions in 0.5 M HCl solution at room temperature

Table 3 Electrochemical properties of HEAs with 1 at% Sn, 3 at% Sn, and 5 at% Sn additions in comparison with the control HEA when polarized in 0.5 mol/L HCl solution at room temperature

	E _{corr} (V)	i _{corr} (A/cm ²) × 10 ⁻⁵	Corrosion Rate (mm/year)	Polarization Resistance (Ω)
Control	-0.30687	1.004	0.1166	3188.3
1 at% Sn	-0.19026	1.9262E-04	0.04238	6462.2
3 at% Sn	-0.24358	6.4343E-05	0.03530	5974.8
5 at% Sn	-0.24094	2.7175E-07	0.02320	8287.09

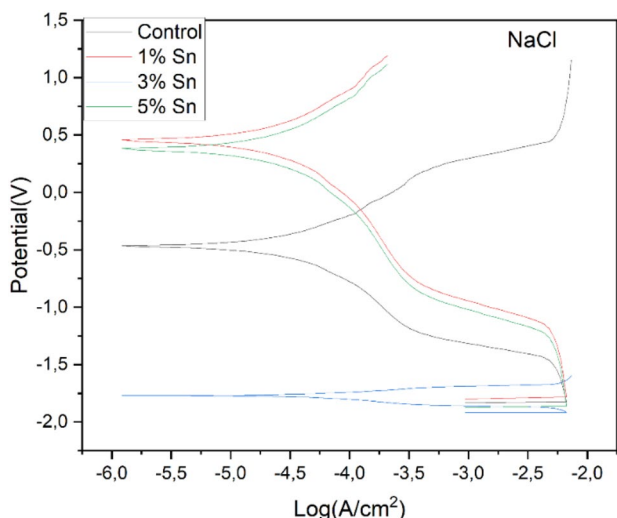


Fig. 9 Potentiodynamic polarization curves of AlCrFeMnNi Control HEA and HEAs with 1 at% Sn, 3 at% Sn, and 5 at% Sn additions in 3.5 at% NaCl solution at room temperature

Table 4 Electrochemical properties of HEAs with 1 at% Sn, 3 at% Sn, and 5 at% Sn additions in comparison with the control HEA when polarized in 3.5 at% NaCl solution at room temperature

	E_{corr} (V)	i_{corr} (A/cm^2) $\times 10^{-5}$	Corrosion Rate (mm/year)	Polarization Resistance (Ω)
Control	-0.47305	2.8666	0.2331	3449.4
1 at% Sn	-0.40207	18.061	0.03594	7414.98
3 at% Sn	-0.68876	233.34	0.31320	2311.3
5 at% Sn	-0.42207	0.55638	0.07114	7027.6

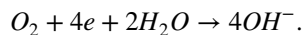
(- 0.24094 V) and smaller i_{corr} ($2.7175E-12 A/cm^2$), which implies superior corrosion resistance as compared to the other alloy samples. This is also demonstrated by its lower corrosion rate of 0.02320 mm/year. The control HEA had a high corrosion rate value of 0.1166 mm/year, and this was proven to diminish with the inclusion of Sn in other alloys. The samples with 1 at% and 3 at% Sn addition had lower deterioration rate compared to the sample without Sn. However, 5 at% Sn additive alloy had a much lower corrosion rate than all of the other alloys, hence, higher resistance to corrosion. This confirms the research of Muangtong, Namus [31], which states that the high corrosion resistance of 5 at% Sn sample can be attributed to the passive film generated at the surface as well as the high Ni-Sn phase corrosion potential [36].

4.2 NaCl Solution

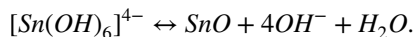
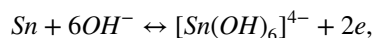
Figure 9 shows the cathodic and anodic polarization curves for HEAs with 1 at% Sn, 3 at% Sn, and 5 at% Sn additions

in contrast to the control HEA in NaCl solution. The corrosion potential (E_{corr}), corrosion potential density (i_{corr}), corrosion rate (mm/year), and polarization resistance (Ω) derived from Tafel data are summarized in Table 4. The addition of 1 at% Sn shows a more positive potential shift compared to that of 0 at% Sn. This can also be explained by its higher E_{corr} (- 0.40207 V) and a lower i_{corr} ($0.00018061 A/cm^2$), indicating that it possesses a higher corrosion resistance than the samples with 0 at%, 3 at% Sn, and 5 at% Sn. This is further evidenced by its decreased corrosion rate of 0.03594 mm/year. Polat and Tekin [19] explain that low levels of Sn segregation are combined with a dense, uniform oxide film that has a good shielding effect to increase the alloy's corrosion resistance. This is supported by the equations written below.

In the neutral and alkaline media, the cathodic reaction is taken place as follows:



The produce OH^- can collaborate in other reactions to form highly coordinated Sn(II) hydroxo-complexes as follows:



The control HEA had a high corrosion rate value of 0.2331 mm/year, which was proven to diminish with the inclusion of Sn in other alloys except for 3 at% Sn. As the amount of Sn increases to 3 at%, the potential swings to the negative side of the control, reflecting a reduction in ability to resist corrosion. However, at 5 at%, the potential returns to the positive side, implying an improvement in polarization resistance. This is because the addition of Sn enhances the durability of the created passive layer, which shields the alloy from degradation due to corrosion. This can also be attributed to the chloro-chromium complexes that develop when Cr is present in NaCl at room temperature. This reduces the alloy's resistance to pitting [50].

4.3 NaOH Solution

The cathodic and anodic polarization curves are shown in Fig. 10. Table 5 summarizes the corrosion potential (E_{corr}), corrosion potential density (i_{corr}), corrosion rate (mm/year), and polarization resistance (Ω) computed from the Tafel and Potentiodynamic curves.

The introduction of Sn reduced the control HEA's high corrosion rate value of 1.168 mm/year in other alloys. There is a positive potential shift when 1 at% Sn is added. The potential swings more positively as the amount of Sn increases, which boosts the HEAs' resistance to corrosion. This can be further

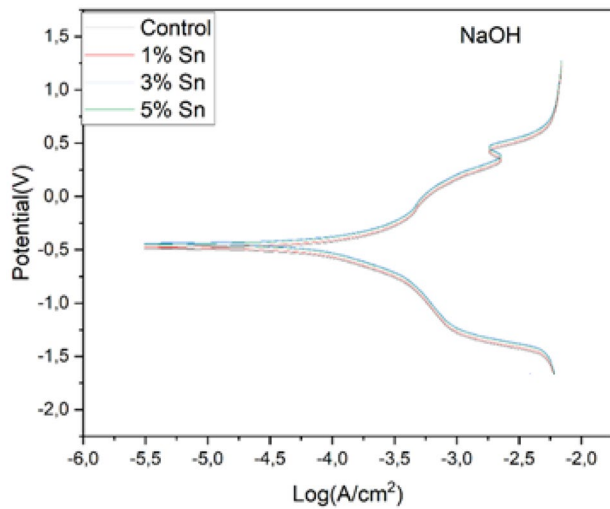


Fig. 10 Potentiodynamic polarization curves of AlCrFeMnNi control HEA and HEAs with 1 at% Sn, 3 at% Sn, and 5 at% Sn additions in 0.5 M NaOH solution at room temperature

Table 5 Electrochemical properties of HEAs with 1 at% Sn, 3 at% Sn, and 5 at% Sn additions in comparison with the control HEA when polarized in 0.5 mol/L NaOH solution at room temperature

	E_{corr} (V)	i_{corr} (A/cm^2) $\times 10^{-5}$	Corrosion Rate (mm/year)	Polarization Resistance (Ω)
Control	-0.50151	74.043	1.168	4753.99
1 at% Sn	-0.47305	42.231	0.07902	7175.2
3 at% Sn	-0.42981	36.515	0.04443	8880.86
5 at% Sn	-0.31516	0.31169	0.026218	9870.29

supported by the Fe–Cr–Mn-rich phases present in the sample with remarkable corrosion resistance [32]. The corrosion rate was lowered in the alloy samples with 1 at% and 3 at% Sn addition compared to the alloy with zero amount of Sn. The sample with 5 at% Sn additions showed a higher E_{corr} (-0.31516 V) and a lower i_{corr} ($3.1169 \times 10^{-6} \text{ A}/\text{cm}^2$) than the samples with 3 at% Sn and 1 at% Sn additions, as well as the control HEA, demonstrating increased corrosion resistance. Its reduced corrosion rate estimation of 0.026218 mm/year adds to this. This could be due to the fact that the presence of Sn makes the resultant HEAs form considerably more solid coatings on the surface of the alloys, shielding the HEAs from contact with the basic environment and increasing their corrosion resistance [51].

The more resistance by the presence of Sn may be attributed to enhance the tin oxide film as protective layers by many reactions as follows:

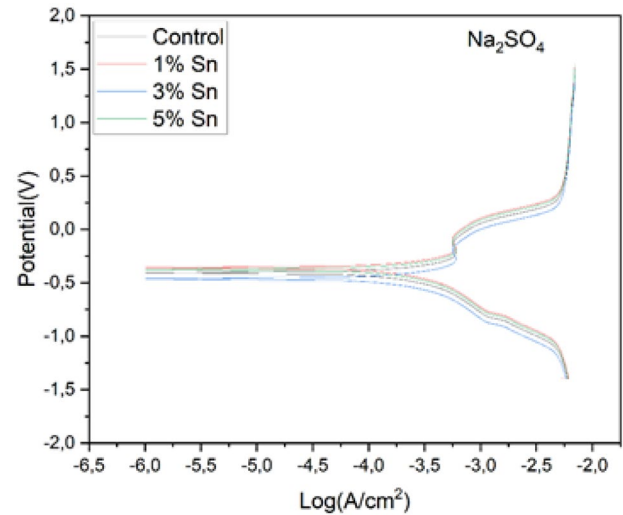
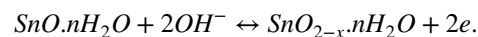


Fig. 11 Potentiodynamic Polarization Curves of AlCrFeMnNi Control HEA and HEAs with 1 at% Sn, 3 at% Sn, and 5 at% Sn Additions in 0.5 M Na_2SO_4 Solution at Room Temperature

Table 6 Electrochemical Properties of HEAs with 1 at% Sn, 3 at% Sn, and 5 at% Sn Additions in Comparison with the Control HEA when Polarized in 0.5 mol/L Na_2SO_4 Solution at Room Temperature

	E_{corr} (V)	i_{corr} (A/cm^2) $\times 10^{-5}$	Corrosion Rate (mm/year)	Polarization Resistance (Ω)
Control	-0.4068	63.654	0.1966	7267.17
1 at% Sn	-0.028421	2.3281	0.02752	15,017
3 at% Sn	-0.56727	0.32563	0.03788	22,109
5 at% Sn	-0.39487	59.235	0.28831	47,322.4



4.4 Na_2SO_4 Solution

Figure 11 presents the cathodic and anodic polarization curves, showing the polarization behavior of Sn-doped HEA samples. Table 6 provides an overview of the corrosion data computed from Tafel curves.

A more negative potential shift is observed with the addition of 1 at% Sn. The sample also had both higher E_{corr} (-0.028421 V) and smaller i_{corr} ($0.00023281 \text{ A}/\text{cm}^2$), which shows better corrosion resistance compared to all the other alloys. This is also proven by its smaller value of corrosion rate of 0.02752 mm/year. This shows that it is more corrosion resistant than other alloys in Na_2SO_4 environment. This may be due the alloy's ability to form much more stable oxide film which enables it to resist interaction with the environment, hence, making it resistant to corrosion. The control HEA had a high corrosion rate value of 0.1966 mm/

year which was shown to decrease in other alloys with the addition of Sn. However, increasing the percentage of Sn has a much more negative potential shift compared to the control and other Sn-containing alloys. This explains the inability of the alloy to form stable passive layers which resist corrosion. Further addition of Sn beyond 3 at% caused the potential to shift negatively, thus, making the HEA resistant to corrosion. This can also be explained by the presence of Cr and Al which supports the stability of oxide films [52].

5 Corrosion SEM/EDS Results

SEM was used to examine the microstructural development during corrosion and determine how adding Sn affected the stability of the AlCrFeMnNi HEA alloy in an acidic and basic environments. Figure 12 shows SEM Micrographs of AlCrFeMnNi HEA samples with different Sn percentages which showed highest resistance to corrosion in HCl, H₂SO₄, NaOH, NaCl, and Na₂SO₄ solutions. On the microstructure of alloy containing 1 at% Sn in HCl solution (Fig. 12a), dark

gray oxide deposits can be seen which could potentially be explained by the aggressiveness of HCl, which can cause the alloy to degrade quickly and lose material, resulting in reduced mechanical qualities. Figure 12b displays the presence of light gray and white layers that are peeling off. On the material's surface, there are also a few tiny pits or holes that can be seen. Sulfuric acid's strong reaction with the alloy's surface may be the cause of this.

Aggressive anions break down the passivating layer on the alloy's surface and cause micro-anodes of active metal surrounded by large cathodic protective areas of the passive metal to be formed. Scaling of the sample surface is apparent on the sample surface with holes and pits on the microstructure of Fig. 12d (3 at% Sn sample in NaCl solution). Perhaps this is owed to the presence of chloride ions from NaCl, which have the capacity to form microscopic pits or holes in the material, resulting in faster corrosion in these locations.

Figure 13 displays EDS Micrographs of AlCrFeMnNi HEA samples with different Sn percentages which showed highest resistance to corrosion in HCl, H₂SO₄, NaOH, NaCl, and Na₂SO₄ solutions. The presence of oxygen may

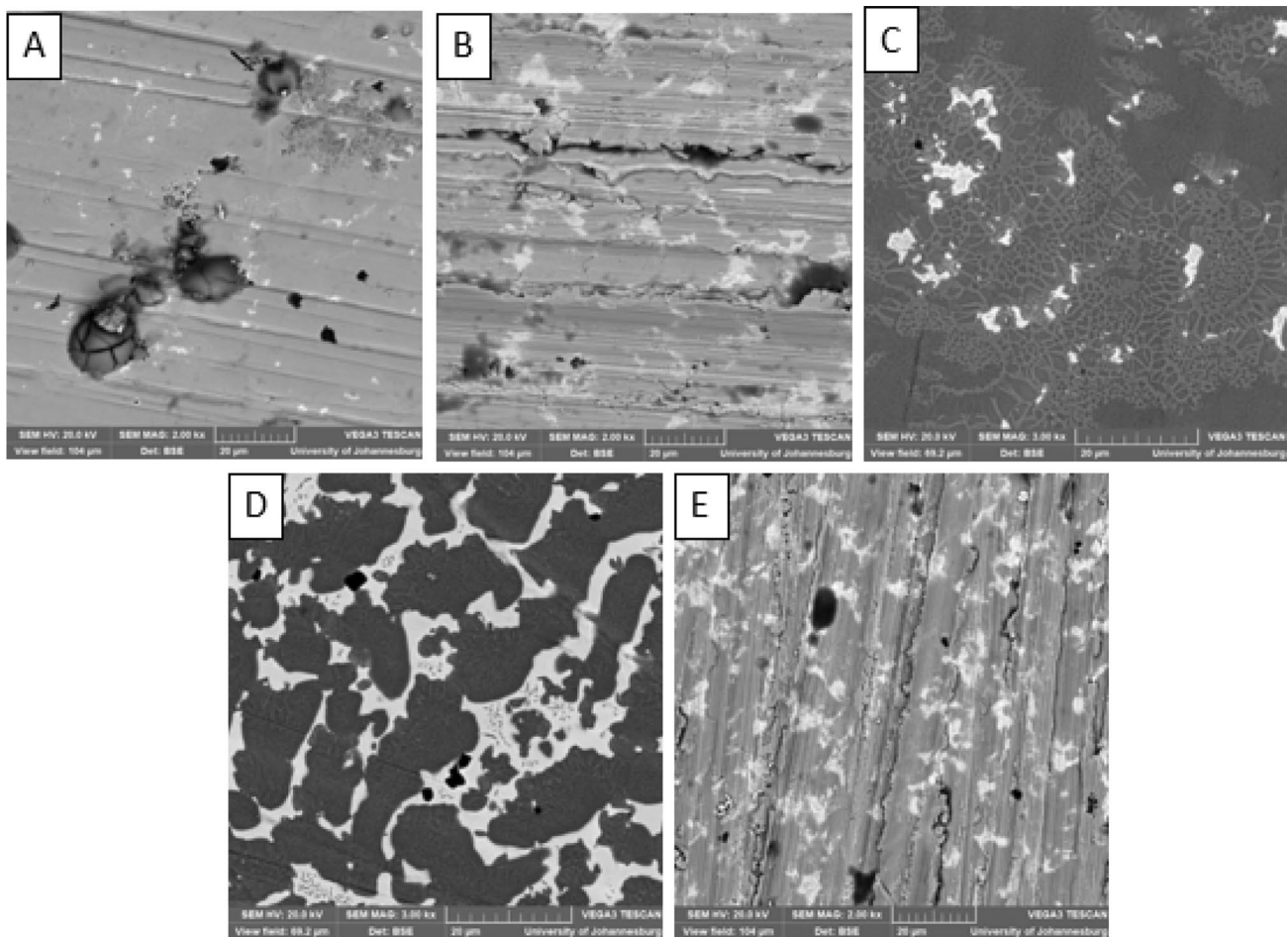


Fig. 12 SEM Micrographs for Corrosion in a) HCl, b) H₂SO₄, c) Na₂SO₄, d) NaOH, and e) NaCl

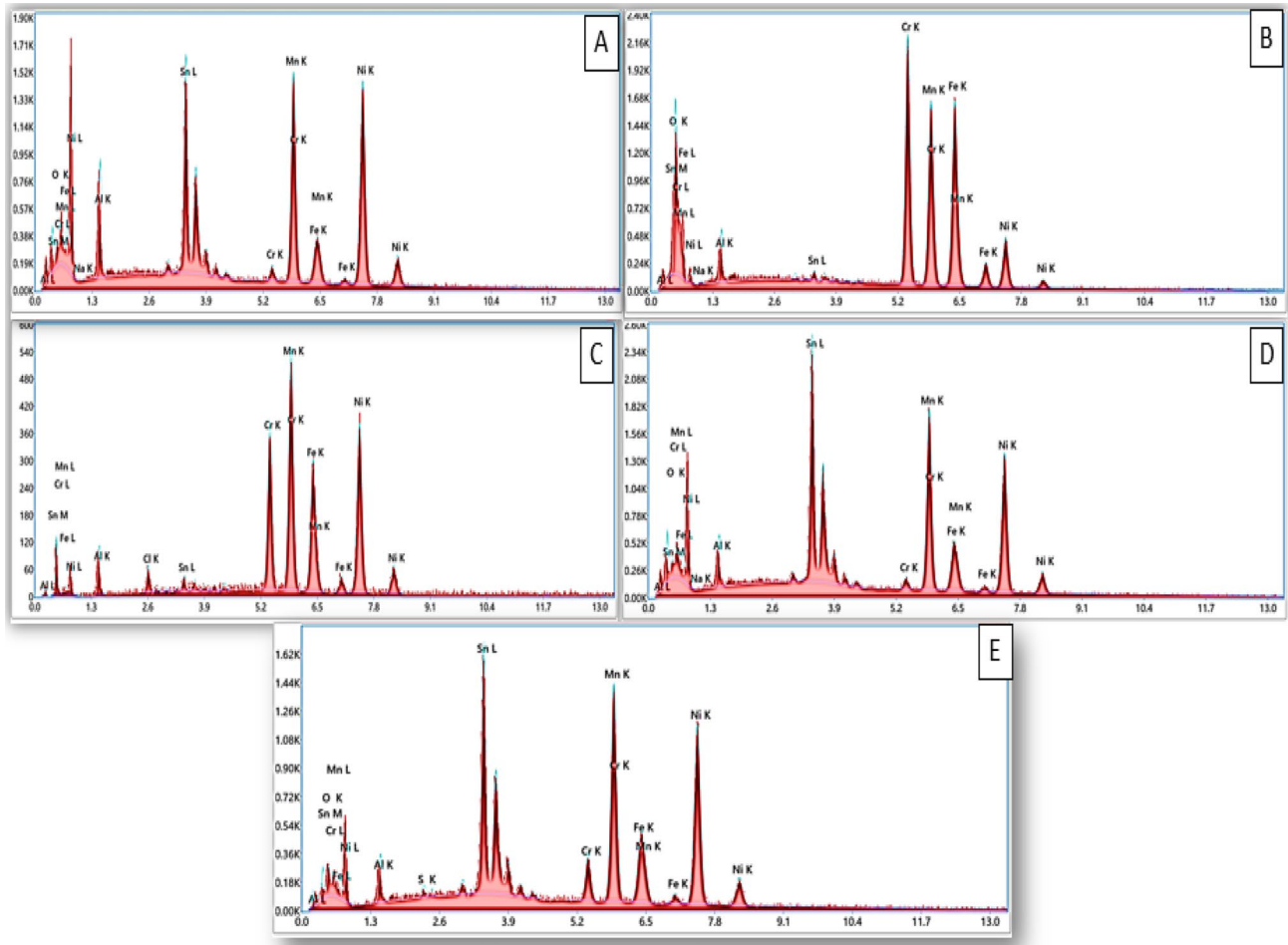


Fig. 13 EDS Micrographs for Corrosion in **A** NaOH, **B** Na₂SO₄, **C** HCl, **D** NaCl, and **e** H₂SO₄ Solution

Table 7 Calculated Weight Loss Results for Control and Sn-Containing HEAs in H₂SO₄ Solution

	Control	1 at% Sn	3 at% Sn	5 at% Sn
5 weeks weight loss	0.2 g	1.22 g	0.32 g	0.16 g
Daily weight loss	0.006 g/day	0.035 g/day	0.009 g/day	0.0046 g/day
Yearly weight loss	2.19 g/yr	12.72 g/yr	3.34 g/yr	1.67 g/yr

be seen in the EDS micrographs. It is possibly due to the fact that Sn can act as an alloying element, giving corrosion resistance by passivating the surface and forming a protective oxide layer. Sulfuric acid may also develop a passive oxide layer on the surface of several metals, including Al and Sn. This oxide layer can operate as a protective barrier, delaying the corrosion process by preventing additional acid-alloy reaction.

6 Weight loss corrosion

6.1 H₂SO₄ solution

Table 7 depicts how several alloys interact with an H₂SO₄ solution environment. When the control HEA was immersed in H₂SO₄ solution for 5 weeks, it lost 2.19 g/year in weight. When compared to the control HEA, adding 1 at% Sn boosted weight reduction by 6 times.

As the amount of Sn increased, the pace of weight loss dropped. The weight loss of 5 at% Sn HEA was much lower than that of the other alloys, at 1.67 g/year. This explains why the 5 at% Sn HEA is so resistant to corrosion.

Figure 14 represents a 3D graphical depiction of the observed weight loss in grams and the computed weight loss percentages of various HEAs in an H₂SO₄ environment over a 5-week period. The percentages of weight loss in all of the HEA samples grow as the duration of time rises. The graph shows that 5 at% Sn has a large increase in weight loss percentage and good corrosion resistance.

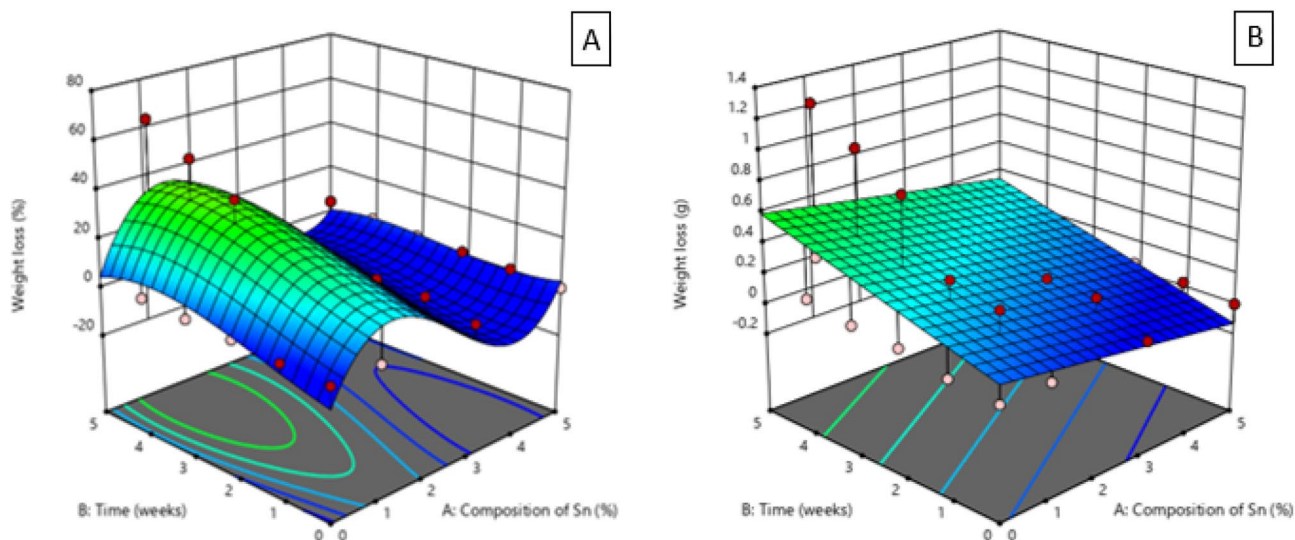


Fig. 14 Weight Loss for Control and Sn-Containing HEAs in H₂SO₄ Solution in **A** Percentage **B** Grams

Table 8 Calculated weight loss results for control and Sn-containing HEAs in NaCl solution

	Control	1 at% Sn	3 at% Sn	5 at% Sn
5 weeks weight loss	0.12 g	0.04 g	0.2 g	0.11 g
Daily weight loss	0.003 g/day	0.001 g/day	0.006 g/day	0.003 g/day
Yearly weight loss	1.25 g/yr	0.42 g/yr	2.09 g/yr	1.15 g/yr

6.2 NaCl Solution

It was discovered that the addition of Sn AlCrFeMnNi HEA samples reduced weight loss in a NaCl environment. Table 8 demonstrates that as the content of Sn gets to 3 at%, it causes a reduction in the alloys' corrosion resistance. This might be due to the alloys' inability to form a stable passive layer that prevents the solution from interacting with the alloy further. As a result, corrosion resistance is lowered because of the development of less protective and uneven passive coatings. However, an increase in Sn to 5 at% results in the reduction of weight loss.

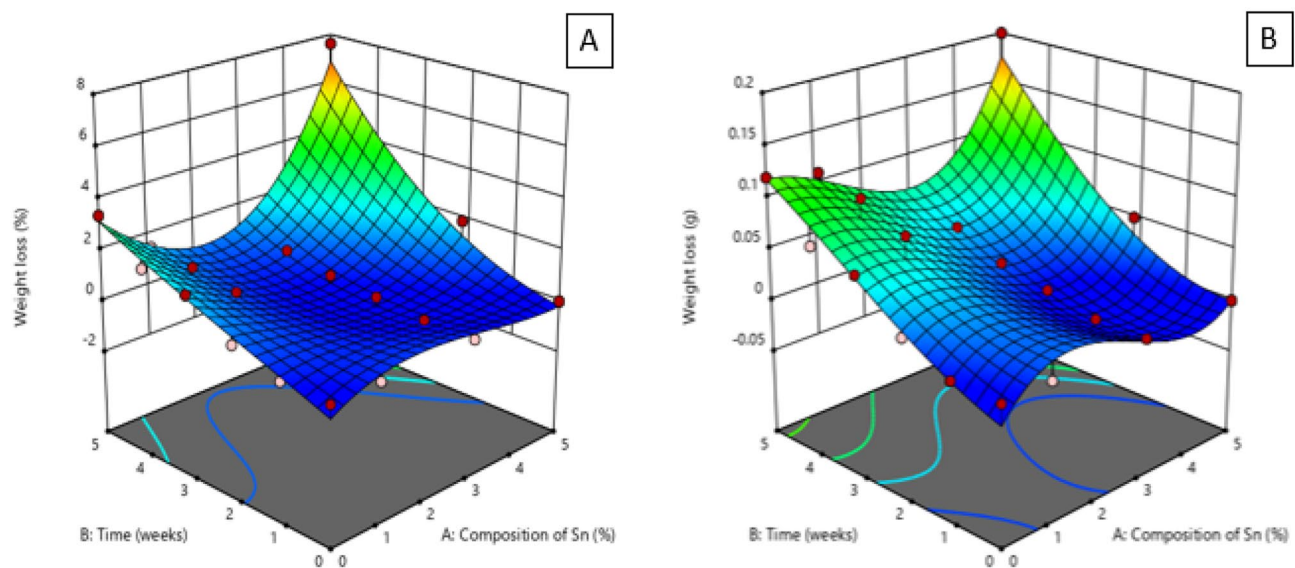


Fig. 15 Weight loss for control and Sn-containing HEAs in NaCl solution in **A** percentage and **B**) grams

Figure 15 shows that 1 at% Sn has a lower weight reduction percentage than other HEAs. This reveals that it has greater corrosion resistance in a NaCl environment when compared to all other alloys. This good attribute is due to the alloy's ability to form a stable passive covering that protects the alloy against corrosion. This oxide layer acts as a barrier, keeping Cl^- ions out and decreasing the rate of corrosion. The 3 at% Sn-modified alloy lost weight at a faster pace than the 1 at% and 5 at% Sn-modified alloys. This might be explained by the existence of intermetallic complexes, which make the 5 at% Sn-modified alloy more sensitive to corrosion attack and cause it to lose weight quicker.

6.3 NaOH Solution

All of the HEA samples remained in NaOH solution for 5 weeks without experiencing any weight reduction. Table 9 and Fig. 16 demonstrate this.

The samples' mass is constant throughout. This might be due to a lack of interaction between the alloy surfaces and the NaOH environment. The alloys can endure not losing electrons into the solution due to their strength. As a result, all alloys are corrosion resistant in a NaOH environment. The presence of Sn in the alloy composition may have contributed to the formation of a protective surface layer that acts as a physical deterrent to the corrosive effects of NaOH solution. This layer protects the alloy from solution penetration while also keeping the alloy's weight stable.

6.4 Statistical modeling

6.4.1 NaCl solution

The Design-Expert Software was used to do statistical modeling. Response surface in two-dimensional plot is displayed in Fig. 17. It is clear that the Sn percentage has the most impact on the rate of weight loss. The relationship between the experimental results and the model's output response variables is depicted in Fig. 18.

The figure demonstrates a strong connection, which supports the validity of using this mathematical modeling to forecast the weight loss characteristics of the Sn-modified HEA samples in NaCl solution. The normalcy assumption is met when the residuals roughly follow a straight line

Table 9 Calculated weight loss results for control and Sn-containing HEAs in NaOH solution

	Control	1 at% Sn	3 at% Sn	5 at% Sn
5 weeks weight loss	0 g	0 g	0 g	0 g
Daily weight loss	0 g/day	0 g/day	0 g/day	0 g/day
Yearly weight loss	0 g/yr	0 g/yr	0 g/yr	0 g/yr

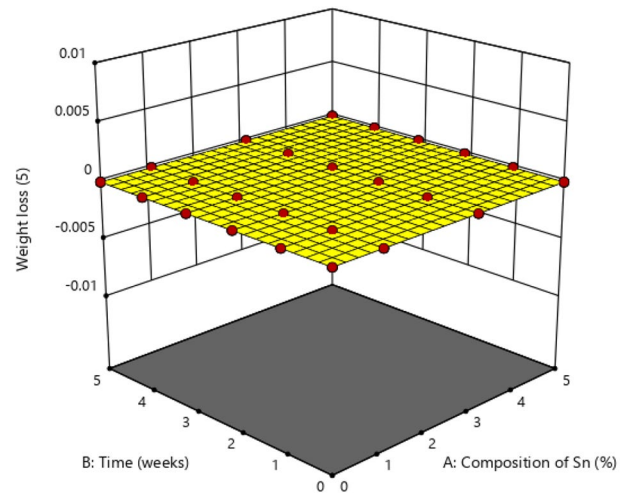


Fig. 16 Weight loss percentages for control and Sn-containing HEAs in NaOH solution

[53]. The normality assumptions for both responses are met since it can be determined that the residuals are normally distributed [54]. The validity of the model was tested using ANOVA analysis of variance, and the degree of significance of the terms was determined using the t test and p values at P 0.05. Table 10 displays the essential model terms as well as the model's F-value from the analysis of variance. The model has an F-value of 30.01, indicating that it is significant [55, 56]. An F-value this big might arise owing to noise just 0.01

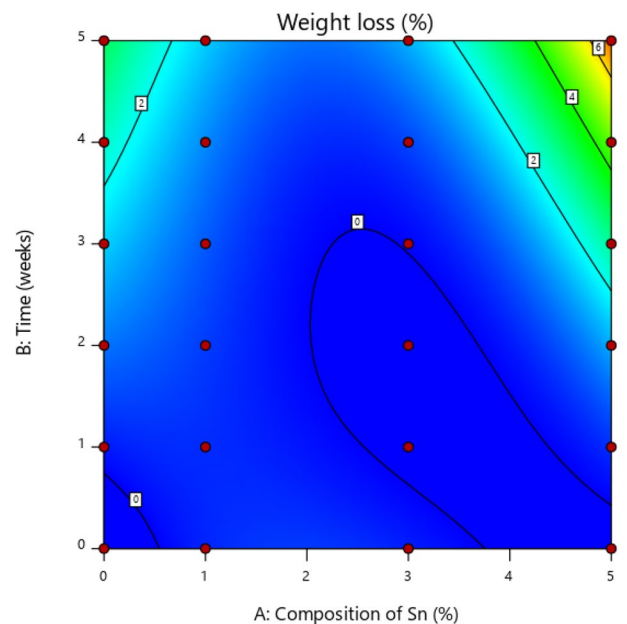


Fig. 17 Two-Dimensional Representation of Weight Loss in NaCl Solution

Fig. 18 ANOVA for Cubic Model for Sn-Containing Samples in NaCl Solution

Design-Expert® Software

Weight loss

Color points by value of Weight loss:

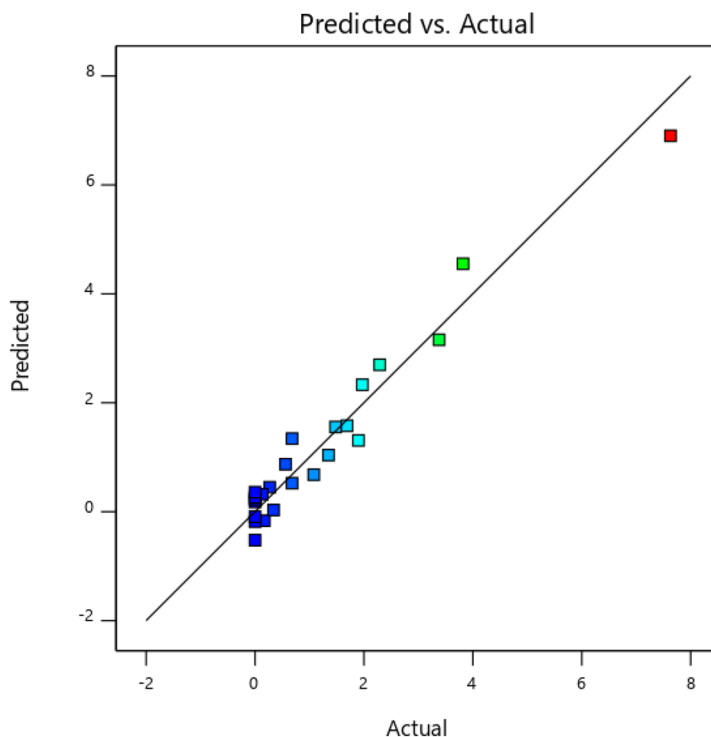


Table 10 Response 1: Weight loss

Source	Sum of Squares	df	Mean Square	F-value	p value	
Model	66.94	9	7.44	30.01	<0.0001	Significant
A-Composition of Sn	0.1043	1	0.1043	0.4209	0.5270	
B-Time	0.0541	1	0.0541	0.2184	0.6474	
AB	4.79	1	4.79	19.31	0.0006	
A ²	11.84	1	11.84	47.77	<0.0001	
B ²	2.14	1	2.14	8.65	0.0107	
A ² B	11.12	1	11.12	44.87	<0.0001	
AB ²	0.9794	1	0.9794	3.95	0.0668	
A ³	0.4307	1	0.4307	1.74	0.2086	
B ³	0.0057	1	0.0057	0.0229	0.8820	
Residual	3.47	14	0.2479			
Cor Total	70.41	23				

at% of the time. Model terms with P values less than 0.0500 are significant. In this situation, the model variables AB, A², B², and A²B are relevant [55, 57].

7 Conclusion

Success has been achieved in the synthesis and modification of AlCrFeMnNi HEA with various Sn concentrations. Sn addition's impact on the modified HEAs' microstructural development, nanohardness, thermal stability, and corrosion behavior was studied. Corrosion testing results in 0.5 M NaOH, 0.5 M HCl, 0.5 M H₂SO₄, 3.5wt% NaCl, and 0.5 M

Na₂SO₄ solutions on all the tin-modified samples, which was done. The corrosion resistance of the 5 at% Sn sample in NaOH solution was higher. The corrosion resistance of the 3 at% Sn sample in NaCl solution was higher. In Na₂SO₄ solution, the 1 at% Sn sample exhibited superior corrosion resistance. The corrosion resistance of the 5 at% Sn sample in HCl solution was higher. In H₂SO₄ solution, the 5 at% Sn sample exhibited greater corrosion resistance. The 5 at% Sn sample had the lowest displacement value of 1668.98 nm, indicating that it has the strongest strength and restricts the passage of indenter forces through the alloy sample. The penetration depth of 5 at% Sn alloy was observed to be lower as compared to 1 at% and 3 at% Sn-modified AlCrFeNiMn

HEA. This may be due to the fact that a higher solid solution tin content of 5 at% can increase solid solution strengthening, resulting in increased hardness and decreased nano-indentation test penetration depth.

Author contributions P.M contributed by doing the experimental setup and completion, writing and interpretation of the journal and experimental data, respectively; N.M contributed by assisting with data interpretation and writing review; M.B.S contributed by providing and advising on parameters optimization procedure and proof reading; L.R.K contributed by interpreting the experimental data and writing review. All authors have read and agreed to the published version of the manuscript.

Funding Open access funding provided by Tshwane University of Technology. No funding was associated with this research.

Declarations

Conflict of interest I declare that the authors have no competing interests as defined by Springer, or other interests that might be perceived to influence the results and/or discussion reported in this paper.

Open Access This article is licensed under a Creative Commons Attribution 4.0 International License, which permits use, sharing, adaptation, distribution and reproduction in any medium or format, as long as you give appropriate credit to the original author(s) and the source, provide a link to the Creative Commons licence, and indicate if changes were made. The images or other third party material in this article are included in the article's Creative Commons licence, unless indicated otherwise in a credit line to the material. If material is not included in the article's Creative Commons licence and your intended use is not permitted by statutory regulation or exceeds the permitted use, you will need to obtain permission directly from the copyright holder. To view a copy of this licence, visit <http://creativecommons.org/licenses/by/4.0/>.

References

- Muangtong P et al (2020) The corrosion behaviour of CoCrFeNi-x (x= Cu, Al, Sn) high entropy alloy systems in chloride solution. *Corros Sci* 172:108740
- Yeh J-W et al (2007) Anomalous decrease in X-ray diffraction intensities of Cu–Ni–Al–Co–Cr–Fe–Si alloy systems with multiprincipal elements. *Mater Chem Phys* 103(1):41–46
- Yeh J-W et al (2004) Formation of simple crystal structures in Cu–Co–Ni–Cr–Al–Fe–Ti–V alloys with multiprincipal metallic elements. *Metall and Mater Trans A* 35:2533–2536
- Tsai K-Y, Tsai M-H, Yeh J-W (2013) Sluggish diffusion in co–cr–fe–mn–ni high-entropy alloys. *Acta Mater* 61(13):4887–4897
- Anne BR et al (2021) A crucial review on recent updates of oxidation behavior in high entropy alloys. *SN Applied Sciences* 3:1–23
- Yang L et al (2019) High He-ion irradiation resistance of CrMn–FeCoNi high-entropy alloy revealed by comparison study with Ni and 304SS. *J Mater Sci Technol* 35(3):300–305
- Kalantari H et al (2023) Nanocrystalline AlCoFeNiTiZn high entropy Alloy: Microstructural, Magnetic, and thermodynamic properties. *Adv Powder Technol* 34(5):104009
- Kumar NK et al (2016) Microstructural stability and mechanical behavior of FeNiMnCr high entropy alloy under ion irradiation. *Acta Mater* 113:230–244
- Alshataif YA et al (2020) Manufacturing methods, microstructural and mechanical properties evolutions of high-entropy alloys: a review. *Met Mater Int* 26:1099–1133
- Wang B et al (2022) General synthesis of high-entropy alloy and ceramic nanoparticles in nanoseconds. *Nature Synthesis* 1(2):138–146
- Li Z et al (2018) Combinatorial metallurgical synthesis and processing of high-entropy alloys. *J Mater Res* 33(19):3156–3169
- Varalakshmi S, Kamaraj M, Murty B (2008) Synthesis and characterization of nanocrystalline AlFeTiCrZnCu high entropy solid solution by mechanical alloying. *J Alloy Compd* 460(1–2):253–257
- Rajendrachari S (2022) An overview of high-entropy alloys prepared by mechanical alloying followed by the characterization of their microstructure and various properties. *Alloys* 1(2):116–132
- Ye X et al (2011) The property research on high-entropy alloy AlxFeCoNiCuCr coating by laser cladding. *Phys Procedia* 12:303–312
- Yin, X. and S. Xu. *Properties and preparation of high entropy alloys*. in *MATEC web of conferences*. 2018. EDP Sciences.
- Chen Y et al (2005) Microstructure and electrochemical properties of high entropy alloys—a comparison with type-304 stainless steel. *Corros Sci* 47(9):2257–2279
- Shi Y, Yang B, Liaw PK (2017) Corrosion-resistant high-entropy alloys: A review *Metals* 7(2):43
- Shi Y et al (2018) Homogenization of AlxCoCrFeNi high-entropy alloys with improved corrosion resistance. *Corros Sci* 133:120–131
- Polat, G., M. Tekin, and H. Kotan, *Role of yttrium addition and annealing temperature on thermal stability and hardness of nanocrystalline CoCrFeNi high entropy alloy*. *Intermetallics*, 2022. **146**: p. 107589.
- Moraes PE et al (2014) Effects of Sn addition on the microstructure, mechanical properties and corrosion behavior of Ti–Nb–Sn alloys. *Mater Charact* 96:273–281
- Chen Y et al (2023) Heavy ion irradiation effects on CrFeMnNi and AlCrFeMnNi high entropy alloys. *J Nucl Mater* 574:154163
- Zhang M et al (2022) Microstructure and elevated temperature wear behavior of laser-cladded AlCrFeMnNi high-entropy alloy coating. *Opt Laser Technol* 149:107845
- Munitz A, Meshi L, Kaufman M (2017) Heat treatments' effects on the microstructure and mechanical properties of an equiatomic Al–Cr–Fe–Mn–Ni high entropy alloy. *Mater Sci Eng, A* 689:384–394
- Feltrin AC et al (2022) Review of Novel High-Entropy Protective Materials: Wear, Irradiation, and Erosion Resistance Properties. *Entropy* 25(1):73
- Liu J et al (2021) The Evolution of Intermetallic Compounds in High-Entropy Alloys: From the Secondary Phase to the Main Phase. *Metals* 11(12):2054
- Zhang Y et al (2014) Microstructures and properties of high-entropy alloys. *Prog Mater Sci* 61:1–93
- Du Y et al (2022) Enhancing the tribological performance of the TiZrHfCuBe high entropy bulk metallic glass by Sn addition. *Tribol Int* 171:107529
- Gu X et al (2020) Microstructure and mechanical properties of CoCrFeMnNiSn x high-entropy alloys. *Met Mater Int* 26:292–301
- Li B et al (2020) Selective laser melting of CoCrFeNiMn high entropy alloy powder modified with nano-TiN particles for additive manufacturing and strength enhancement: Process, particle behavior and effects. *Powder Technol* 360:509–521
- Liu L et al (2013) Microstructure and tensile properties of FeMn–NiCuCoSnx high entropy alloys. *Mater Des* 44:223–227

31. Muangtong P, Namus RM, Goodall R (2020) Improved tribocorrosion resistance by addition of Sn to CrFeCoNi high entropy alloy. *Metals* 11(1):13
32. Grünebohm A, Herper HC, Entel P (2016) On the rich magnetic phase diagram of (Ni, Co)–Mn–Sn Heusler alloys. *J Phys D Appl Phys* 49(39):395001
33. Dewangan SK et al (2020) Synthesis and characterization of hydrogenated novel AlCrFeMnNiW high entropy alloy. *Int J Hydrogen Energy* 45(34):16984–16991
34. Nguyen TD, Zhang J, Young DJ (2016) Effect of Mn on oxide formation by Fe-Cr and Fe-Cr-Ni alloys in dry and wet CO₂ gases at 650° C. *Corros Sci* 112:110–127
35. Bachagha, T., et al., *Microstructure characterization, structure and magnetic properties of Ni–Mn–Sn shape memory alloys*. *Journal of Thermal Analysis and Calorimetry*, 2021: p. 1–8.
36. Hao X et al (2022) Effect of Sn addition on the tribological behaviors of CoCrFeNi high entropy alloys. *J Alloy Compd* 909:164657
37. Sankaran, E.M. and A. Sonachalam, *Exchange Bias Effect in Ni-Mn Heusler Alloys*. *Metastable, Spintronics Materials and Mechanics of Deformable Bodies-Recent Progress*, 2020: p. 133.
38. Ludwig A et al (2004) MEMS tools for combinatorial materials processing and high-throughput characterization. *Meas Sci Technol* 16(1):111
39. Büsgen T et al (2004) Ab initio calculations of structure and lattice dynamics in Ni– Mn– Al shape memory alloys. *Phys Rev B* 70(1):014111
40. Wittmann, M., I. Baker, and J. Hanna, *Microstructure and mechanical properties of Fe-Ni-Mn-Al alloys*. *MRS Online Proceedings Library (OPL)*, 2004. **842**: p. S5. 17.
41. Rahimi R et al (2014) Microstructure and mechanical properties of Al-alloyed Fe–Cr–Ni–Mn–C stainless steels. *Mater Sci Eng, A* 618:46–55
42. Sánchez-Alarcos V et al (2011) Structural and magnetic properties of Cr-doped Ni–Mn–In metamagnetic shape memory alloys. *J Phys D Appl Phys* 44(39):395001
43. Sun Z et al (2014) Microstructure and the properties of AlFeCoNi–CrSn x high-entropy alloys. *Arab J Sci Eng* 39:8247–8251
44. Li T et al (2023) Corrosion Behavior of High Entropy Alloys and Their Application in the Nuclear Industry—An Overview. *Metals* 13(2):363
45. Liu L et al (2012) Microstructure and the properties of FeCoCu–NiSn_x high entropy alloys. *Mater Sci Eng, A* 548:64–68
46. Botero C et al (2012) Nanoindentation of Al₂O₃/Al₂TiO₅ composites: Small-scale mechanical properties of Al₂TiO₅ as reinforcement phase. *J Eur Ceram Soc* 32(14):3723–3731
47. Demirtaş, H., M. Riyadh, and R. Anaee, *Wear and Corrosion Properties for the Effect of Addition Cu to Ti–18Nb Biomaterial*. *Chemistry Africa*, 2023: p. 1–9.
48. Naser SA, Anaee RA, Jaber HA (2023) Deposition of GdSmTi Coating for Corrosion Control of ????? ?????? Bio-Field Engineering and Technology Journal 41(06):836–844
49. Maged SAA, Anaee RA, Mathew MT (2023) The Role of Uric Acid to Reduce the Corrosion of Co-Cr-Mo Alloy as Joint in Presence of Ca and Vitamin D3. *Journal of Bio-and Tribo-Corrosion* 9(4):66
50. Chen R et al (2018) Composition design of high entropy alloys using the valence electron concentration to balance strength and ductility. *Acta Mater* 144:129–137
51. Zheng Z et al (2015) Microstructure and corrosion behaviour of FeCoNiCuSn_x high entropy alloys. *Mater Sci Technol* 31(10):1148–1152
52. Swanson, O.J., *Corrosion of high-entropy alloys in chloride solutions*. 2018, The Ohio State University.
53. Ogunbiyi O et al (2020) Optimization of spark plasma sintering parameters of inconel 738LC alloy using response surface methodology (RSM). *International Journal of Lightweight Materials and Manufacture* 3(2):177–188
54. Bradley, N., *The response surface methodology*. 2007, Indiana University South Bend.
55. Myers RH, Khuri AI, Carter WH (1989) Response surface methodology: 1966–1988. *Technometrics* 31(2):137–157
56. Myers RH et al (2004) Response surface methodology: a retrospective and literature survey. *J Qual Technol* 36(1):53–77
57. Khuri AI, Mukhopadhyay S (2010) Response surface methodology. *Wiley Interdisciplinary Reviews: Computational Statistics* 2(2):128–149

Publisher's Note Springer Nature remains neutral with regard to jurisdictional claims in published maps and institutional affiliations.